CrossMark

High-temperature oxidation of HVOF thermally sprayed NiCr–Cr$_3$C$_2$ coatings: microstructure and kinetics

Y. Ding[1] · T. Hussain[1] · D. G. McCartney[1]

Abstract In this study, 25 wt% Ni(Cr)–75 wt% Cr$_3$C$_2$ powder was thermally sprayed onto 304 stainless steel substrate to produce coatings of ~400-µm thick and the oxidation behaviour of the coatings was investigated. The kinetic behaviour of oxidation of freestanding coatings was investigated over short times at 650, 700 and 800 °C using the thermogravimetric analysis technique. The oxidation rate for all samples was parabolic in nature and the parabolic rate constant (k) increased with increasing temperature. The activation energy (Q) for oxidation was found to be around 226 kJ mol^{-1}. Furnace oxidation tests were also carried out on the as-sprayed samples at 700 and 800 °C in laboratory air for times ranging from 1 h up to 16 days (384 h). The oxide scale growth, morphology and phase formation were investigated using scanning electron microscopy, energy dispersive X-ray analysis and X-ray diffraction. An oxide scale covered the surface of the cermet coating following oxidation at both 700 and 800 °C; the scale was significantly thicker at the higher temperature. It was found to be Cr$_2$O$_3$ and it covered both the metal matrix and the Cr$_3$C$_2$ particles present in the coating. The oxide grains had an angular shape after 16 days of exposure at both temperatures but the grain size was significantly larger after exposure at 800 °C.

✉ T. Hussain
tanvir.hussain@nottingham.ac.uk

1 Division of Materials, Mechanics & Structures, Faculty of Engineering, University of Nottingham, Nottingham NG7 2RD, UK

Introduction

The rising global population, the increasing energy demand and concerns about the environment have put significant pressure on the power generation industry to produce electricity more efficiently with reduced CO$_2$ emissions [1, 2]. Growing concern over the effects of CO$_2$ emissions and global warming means that the traditional trend towards the development and use of power plants with ever increasing efficiencies is now being coupled to the use of a wider range of fuels designed to minimise CO$_2$ emissions. Generally, conventional fossil fuel-fired power plants are considered to be a major contributor to CO$_2$ emissions, whereas alternative solid fuels which include biomass and waste products can be classified as *CO$_2$ neutral*. Such fuels can be used alone or co-fired with conventional fossil fuels [3, 4].

Therefore, to meet the targets of reduced CO$_2$ emissions, industry is increasingly moving towards higher steam temperatures and pressures (and hence higher efficiencies) as well as using more biomass fuels. The increased operating temperatures, coupled with biomass-derived flue gases, can give rise to problems of increased steam oxidation inside boiler tubes and pipes and more aggressive external fireside corrosion involving high-temperature oxidation/corrosion of heat exchangers (e.g. waterwalls, superheaters and reheaters) in the power plant. Indeed, there is a strong possibility that the modified operating environments and higher temperatures of operation will cause severe corrosion problems for established heat exchanger materials such as grade 15Mo3 steel, ferritic-martensitic grade 91 type steel and austenitic stainless steel (e.g. type AISI 304) [5].

There is thus considerable interest in protecting these materials from fireside corrosion and erosion-corrosion

(specifically in fluidised bed boilers) using surface engineering routes. In a number of applications, thermally sprayed coatings are being considered as an economic means to provide suitable protection to heat exchangers in biomass fuel-fired boilers and advanced ultra-supercritical (A-USC) power plants operating at steam temperatures up to 760 °C. For example, nickel–chromium coatings have been shown to provide good resistance to high-temperature steam oxidation/corrosion whist NiCr–Cr_3C_2 cermet coatings are of interest in applications where combined resistance to solid particle erosion and oxidation/corrosion is required [6, 7]. It has been reported that NiCr–Cr_3C_2 cermet coatings can operate in aggressive environments at service temperatures up to 900 °C as they have high hardness and good resistance to combined erosion and chemical degradation at elevated temperatures [7–13].

High velocity oxy-fuel (HVOF) thermal spraying is seen as one of the most attractive processes for depositing NiCr–Cr_3C_2 coatings due to its ability to achieve thick (>250 μm), low-porosity (<2 %), well-bonded (bond strength >60 MPa) coatings. This is because, in comparison with other thermal spray processes, the HVOF process can accelerate the particles to high velocities (>500 m s^{-1}) with relatively low particle temperatures in order to minimize chemical degradation of the powder in the spray plume. Whilst many researchers have demonstrated that HVOF thermal spraying can produce good quality NiCr–Cr_3C_2 coatings which display good erosive wear properties at elevated temperature [7–12], knowledge of the high-temperature hot corrosion behaviour of such coatings and the mechanisms involved is still rather limited [14–16]. Indeed, even the topic of high-temperature oxidation behaviour, in air, of HVOF sprayed NiCr–Cr_3C_2 coatings (which will underpin our comprehension of the mechanisms of fireside corrosion, erosion-corrosion and steam oxidation in fossil fuel power plants) has seen relatively little work [17–21].

Therefore, the overall aims of the present study were twofold. First, to investigate the oxidation behaviour, at temperatures between 650 and 800 °C, of HVOF-sprayed coatings deposited using 25 wt% Ni20Cr–75 wt% Cr_3C_2 powder and a liquid fuel HVOF gun. Secondly, to elucidate the formation of the oxide scale on these complex, multi-phase coatings using scanning electron microscopy (SEM) and X-ray diffraction (XRD). In the work reported, coatings were deposited onto 304 stainless steel substrates (a candidate heat exchanger material) and the high-temperature oxidation behaviour of both coated samples and free standing NiCr–Cr_3C_2 coatings was investigated in the temperature range of 650–800 °C. Short-term oxidation of the freestanding coatings was investigated using thermogravimetric analysis (TGA) and longer term furnace oxidation tests of coated samples were undertaken for up to 384 h.

Experimental procedure

Materials and coating process

A commercially available agglomerated and sintered 25 wt% Ni20Cr–75 wt% Cr_3C_2 powder supplied by Praxair Surface Technologies (catalogue number 1375 VM) with a near-spherical morphology and a nominal size range of 15–45 μm was employed in this work. It was sprayed, by a Met-Jet II HVOF thermal spray system (Metallisation Ltd., UK), onto AISI 304 stainless steel substrates of dimensions 58 × 25 × 2 mm. The AISI 304 stainless steel had a nominal composition Fe–19.0Cr–9.3 Ni–0.05C (in wt%). The substrates were grit blasted with brown alumina of mean diameter of ∼250 μm and then cleaned prior to spray deposition. The Met-Jet II is a liquid-fuel thermal spraying system in which kerosene (liquid fuel) is combusted with oxygen gas and nitrogen is used as a carrier gas for the powder. The substrates were mounted on the circumference of a turntable which had a vertical axis of rotation. The rotation speed was set to impart a surface velocity to the substrates of approximately 1 m s^{-1} across the spray path. The gun was positioned in front of the rotating turntable, aligned to give a spray path perpendicular to the rotation axis and set to the required stand-off from the surface of the substrates. It was then scanned vertically up and down at 5 mm s^{-1} (corresponding to an interpass step of approximately 4 mm) to build up a coating of the required thickness. Typically, 25 passes were employed to achieve deposits approximately 400-μm thick. During and after deposition, air jets were directed towards the rotating substrates to provide cooling and maintain the substrate temperature below 200 °C. The spraying parameters were as follows: kerosene flow rate 0.435 L min^{-1}; oxygen flow rate 900 L min^{-1}; carrier gas (N_2) flow rate 6 L min^{-1}; powder flow rate ∼60 g min^{-1}; nozzle length of the spray gun 100 mm and stand-off distance 355 mm.

In order to prepare freestanding samples for oxidation tests, coatings were sprayed (using the same procedure as describe above) onto stainless steel substrates that had been ground with 1500 grit size SiC paper (instead of being grit blasted) and then cleaned. Following spray deposition, these coated substrates were carefully bent around a mandrel which caused the coatings to debond giving freestanding coatings.

High-temperature oxidation tests

The high-temperature oxidation behaviour, in air, of the NiCr–Cr_3C_2 deposits was investigated through two complementary procedures: (a) thermogravimetric analysis of samples cut from freestanding coatings to study the

oxidation kinetics at short times at 650, 700 and 800 °C; and (b) longer term oxidation tests for up to 16 days at 700 and 800 °C to investigate the oxide scale growth and the scale morphology on the NiCr–Cr_3C_2 coatings which had been deposited onto the grit-blasted stainless steel substrates.

Thermogravimetric analysis (TGA)

TGA of the freestanding NiCr–Cr_3C_2 coatings was investigated using a TA instruments Q600 thermogravimetric analyser. To prepare samples for TGA analysis, a square section of dimensions approximately 3 × 3 mm was cut from a freestanding coating (which was ∼400-µm thick) using a precision diamond-tipped cutting disk. The specimens were cleaned using alcohol, dried and weighed using a precision balance. The total surface area of each of the TGA samples was also measured using a micrometer. The oxidation tests were then carried out in commercial grade bottled air (flow rate of 10 mL min^{-1}) at 650, 700 and 800 °C. Samples were held in a recrystallised alumina pan and heated at a rate of 50 K min^{-1} to the test temperature. They were maintained at the test temperature for 3 h before being cooled down to room temperature, also at a rate of 50 K min^{-1}. The change in mass versus time throughout the thermal cycle was recorded for each of the TGA runs. At each temperature, three tests were performed, using a different freestanding sample for each test. Mean values were then used to determine the oxidation kinetics at each temperature.

Longer term furnace oxidation tests

The stainless steel substrates which had been coated with the NiCr–Cr_3C_2 powder to a thickness of ∼400 µm were heat treated in laboratory air at 700 and 800 °C for up to 16 days. In these experiments, the exposed coating surface was in the as-sprayed condition, i.e. no prior surface grinding or polishing had been undertaken. The samples were taken out of the furnace after the following times: 1, 48 h (2 days), 192 h (8 days) and 384 h (16 days). Following the high-temperature exposure, the coated samples were air cooled to room temperature. These samples were used for subsequent microstructural analysis, employing XRD and SEM, to study the coating, the oxide and the oxide morphology.

## Microstructural characterisation

A FEI XL30 (FEI Europe, Eindhoven, The Netherlands) SEM operated at 20 kV was employed to investigate powder, coating and oxide microstructures in cross section as well as the oxide morphology and topography on the top

surface of oxidised coatings. Secondary electron (SE) and backscattered electron (BSE) signals were used to form images as required. For microstructural analysis, powder or coating samples were mounted in conducting resin, ground and diamond polished to a 1-µm finish. To obtain coating cross sections for examination, sprayed samples were sectioned transversely with a SiC slitting wheel, mounted in conducting resin and ground and polished. Semi-quantitative energy dispersive X-ray (EDX) analysis was also carried out in the SEM to aid in phase identification. Powders and coatings were also investigated by XRD using a Bruker D500 X-ray diffractometer with a diffracted-beam monochromator/scintillation counter detector. The instrument was operated at 40 kV and 20 mA to generate Cu K$_\alpha$ radiation at a wavelength of 0.1540 nm. The XRD scans were performed with a step size of 0.02° and a 4 s counting time per step for a 2θ range of 20° to 100°. Typical coated samples for the XRD studies had a surface area of 15 by 5 mm and were 2 mm thick. The coatings were examined both in the as-sprayed condition and following high-temperature exposure at 700 and 800 °C for various times.

Results

Microstructure of the powder and the as-sprayed coating

The XRD pattern obtained from the powder is shown in Fig. 1. It is clear that Cr_3C_2 is a prominent phase with peaks that match closely to those given for Cr_3C_2 in the JCPDS powder diffraction file (00-035-0804). The strong peaks at ∼44.5° and 52° match closely to the peaks
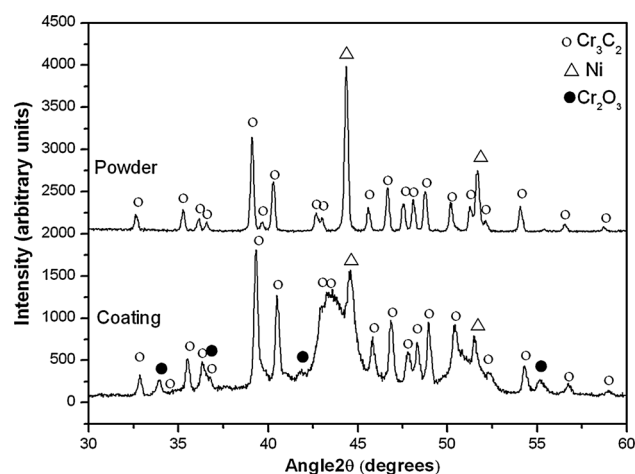

Fig. 1 X-ray diffraction patterns obtained from the 25 %NiCr–75 %Cr_3C_2 agglomerated and sintered powder and the top surface of the as-sprayed coating showing an enlarged view of the 2θ range 30°–60°

expected from fcc Ni (00-004-0850) although the lattice parameters are ~0.002 nm larger than those from pure Ni, which is consistent with these peaks arising from the fcc matrix phase of the powder, which is a Ni–Cr alloy with nominally 20 wt%Cr. There is no evidence for any Cr_2O_3 phase in the powder which indicates that, if present, it was below the limit of detection for XRD which is around 1–2 wt%. The near-spherical morphology of the agglomerated and sintered powder is shown in Fig. 2a and the microstructure of a typical powder particle is displayed in the SEM micrographs of particle cross sections in Fig. 2b, c. The angular, dark contrast features (labelled C) were found to be Cr and C- rich by EDX analysis and so they are presumably the Cr_3C_2 phase identified by XRD. The bright contrast matrix phase was found to be rich in Ni and Cr by EDX analysis (with approximately 20 wt%Cr) and presumably corresponds to the fcc phase with a lattice parameter close to that of pure Ni seen in the XRD pattern of Fig. 1. This powder is evidently composed of porous particles as it had not been plasma densified during manufacture. The lack of connectivity of the metal and ceramic is typical for this type of thermal spray feedstock [22, 23].

The XRD pattern obtained from the top surface of the as-deposited coating is also shown in Fig. 1. It is evident that Cr_3C_2 is still a major phase in the sprayed coating along with an fcc phase with a lattice parameter close to that of nickel. However, for the two peaks labelled as Ni in Fig. 1, the intensity of diffraction is considerably reduced in the pattern obtained from the coating in comparison with that from the feedstock powder. Furthermore, a broad diffraction halo has formed around the region $2\theta = 42.5°$ to 44.5° in the pattern obtained from the coating top surface. A broadened diffraction halo is normally attributed to the presence of amorphous/nanocrystalline material and so the data in Fig. 1 strongly suggest that the Ni-rich matrix phase has become, at least in part, amorphous or nanocrystalline as a consequence of the partial melting and rapid solidification (on impact with the substrate) of the powder particles that takes place during HVOF spraying. The solid circular symbols in Fig. 1 correspond to the peak positions expected from the presence of Cr_2O_3 phase (JCPDS 00-038-1479) and it is clear that there are identifiable oxide phase peaks in the pattern from the coating which are not seen in the powder. These oxide peaks suggest that a small amount of oxide is formed during spraying but it must be remembered that the X-rays penetrate only approximately the 5 μm of the coating and the as-sprayed surface may have a higher oxide level than the coating interior as the former was the last layer to be deposited.

The microstructure of the coatings is shown in the BSE micrograph of coating cross sections in Fig. 3. The
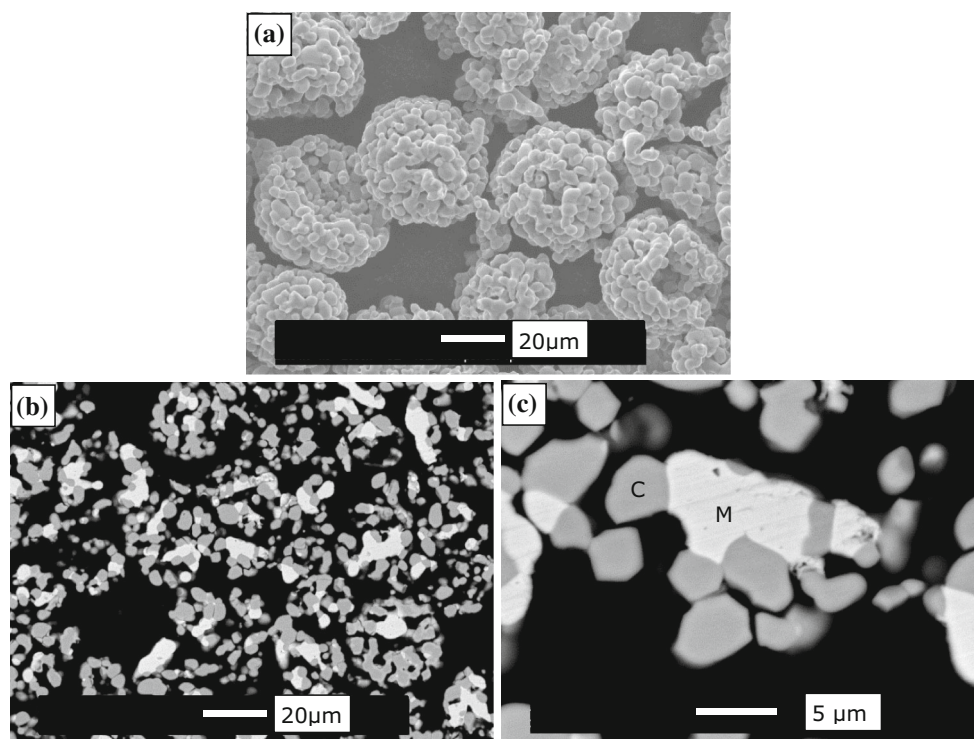
Fig. 2 **a** SE image showing the morphology of the 25 %NiCr–75 %Cr_3C_2 agglomerated and sintered powder; **b** BSE image of a powder particle cross section showing dark contrast Cr_3C_2 grains and bright contrast Ni(Cr) metallic regions, **c** high magnification cross-sectional BSE image showing dark contrast Cr_3C_2 grain (C) and bright contrast Ni(Cr) metallic region (M)
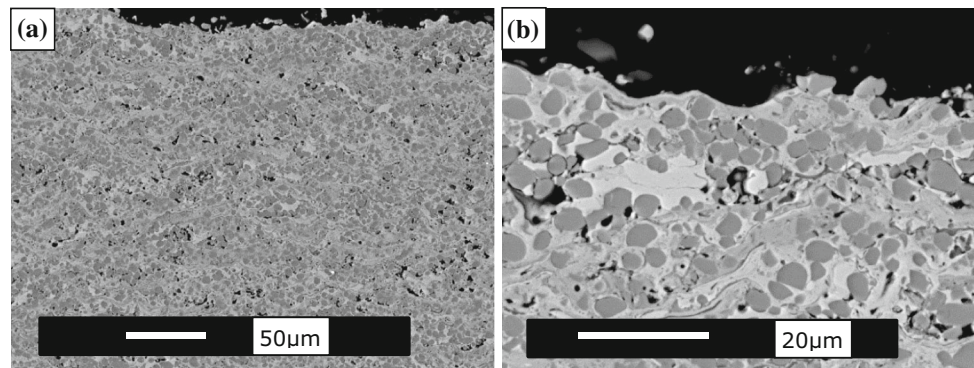
Fig. 3 BSE images of the cross section of the as-sprayed 25 %NiCr–75 %C$_3$C$_2$ coating: **a** low magnification image showing *dark grey*, angular chromium carbide, *light grey* nickel-rich matrix and porosity (*black*); **b** higher magnification image of the top section of the coating in which angular carbides and matrix are more clearly visible

coatings had an average thickness of approximately 400 μm and there was no evidence for cracking of the coating. The lower magnification image, Fig. 3a shows dark grey contrast particles which are relatively uniformly distributed throughout the coating; these are presumed to be the Cr$_3$C$_2$ phase identified by XRD. The lighter grey matrix is presumably a Ni-rich matrix. There is evidence for a small amount of fine scale porosity (small black features) which is also relatively uniformly distributed. The fractions of carbide and porosity revealed in the cross-sectional images are within the range typically seen in HVOF- sprayed coatings of this type [23–28]. The higher magnification image of Fig. 3b shows that the size of dark grey contrast particles ranges from around 3–6 μm. This is similar in size to that seen in the powder (Fig. 2c) but the particles are seen to be more rounded and less angular in nature. EDX analysis showed that the dark angular particles were Cr and C rich with typically <5 % Ni which would seem to confirm that they are indeed the Cr$_3$C$_2$ phase identified by XRD. Their size and rounded morphology suggests that the build-up of the coating, in successive passes of the spray gun, arises from the impact of powder feedstock particles that are heated but only partially melted during spraying. The matrix is seen to exhibit variations in contrast in BSE imaging which suggests variations in mean atomic number i.e. in composition. Because of the fine-scale nature of the coatings, accurate EDX measurements of these different contrast areas were not possible. However, the lighter matrix areas showed consistently lower Cr content than the darker matrix area. The EDX system used could not measure reliably levels of carbon. The variation in contrast in the matrix, probably due to different amounts of dissolved Cr and C, arises from the melting or partial melting of the metal matrix during spraying of the powder and the partial dissolution of the carbide particles into the molten metallic phase in the time of approximately 3–5 ms that particles spend in the spray

plume. These features are in line with other observations from a number of other studies on this system [23–28]. A few thin, dark contrast stringers can also be seen in Fig. 3b and these are probably oxides which form at splat boundaries during spray deposition. This is consistent with the appearance of low intensity but detectable chromium oxide phase peaks in the XRD pattern of Fig. 1.

Oxidation kinetics

Figure 4 illustrates the plots of mass gain per unit area ($\Delta m/a$) versus time of exposure during 3 h TGA experiments (after the set temperature was attained) of the freestanding coatings in an atmosphere of bottled air at 650, 700 and 800 °C. The mass change data suggest the rate could be parabolic in nature for the test temperatures investigated in this study. A parabolic oxidation rate can be
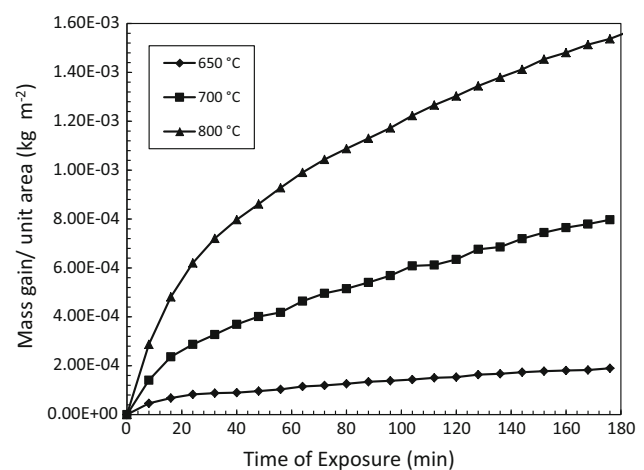
Fig. 4 Plots of mass gain per unit area versus exposure time for 25 %NiCr–75 %Cr$_3$C$_2$ coating at temperatures of 650, 700 and 800 °C ($t = 0$ corresponds to the time when the sample reached the set temperature) obtained from the TGA experiments

represented by the following equation, where t is oxidation time and k and C represent oxidation kinetic constants:

$$(\Delta m/a)^2 = kt + C. \tag{1}$$

The plots of $(\Delta m/a)^2$ versus time of exposure for three temperatures from experiment #1 in Table 1 (as an example) are shown in Fig. 5. Straight lines passing through the origin can be fitted to the data points from the TGA experiments at all three temperatures and all show a single parabolic stage which indicates that oxidation is controlled by diffusion processes in the scale [29]. In all three graphs in Fig. 5 the values of R^2, co-efficient of determination, are above 0.99 which indicate the goodness of fit of the data to a straight line with little scatter. The slopes of the fitted straight lines (i.e. the values of k in Eq. 1) are presented in Table 1. As the TGA experiments at each temperature were repeated three times with three separate freestanding coatings all the measured k values are reported along with a mean value at each temperature. Based on these k values for different test temperatures, an Arrhenius-type plot of ln k versus $10^4/(RT)$, where T is absolute temp and R is the universal gas constant, was constructed as shown in Fig. 6. From the slope of this plot the, the activation energy, Q, for the oxidation of HVOF sprayed 25 % NiCr–75 %Cr$_3$C$_2$ coating is calculated to be $\sim$226 kJ mol^{-1}.

Microstructure of the oxidised coating following high-temperature exposure in air

X-ray diffraction analysis to determine phases present

XRD patterns obtained from the coating top surfaces exposed to a temperature of 700 and 800 °C from 1 h to 16 days are shown in Fig. 7a, b, respectively. The XRD pattern of the as-sprayed coating is also presented in Fig. 7a as a reference. At both 700 and 800 °C, the broad diffraction halo between 40° and 45°, seen in the pattern obtained from the as-sprayed coating, is not evident even after only 1 h of heat treatment. The main effect of the heat treatment is evidently to produce peaks corresponding to Cr$_2$O$_3$ at 2θ values of 24.7°, 33.8°, 36.3° and 54.9° and to allow low-intensity peaks from Cr$_3$C$_2$ at $2\theta = 42.5$° to 43° to become visible.

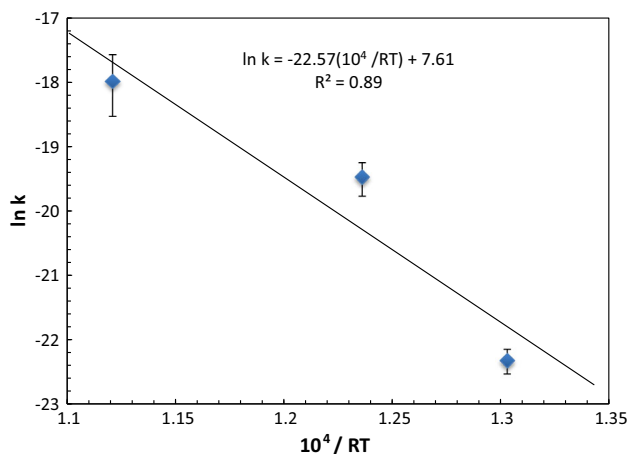After extended ageing in air, the XRD patterns obtained from the top surface show an increased intensity of the

(a)

(b)

(c)
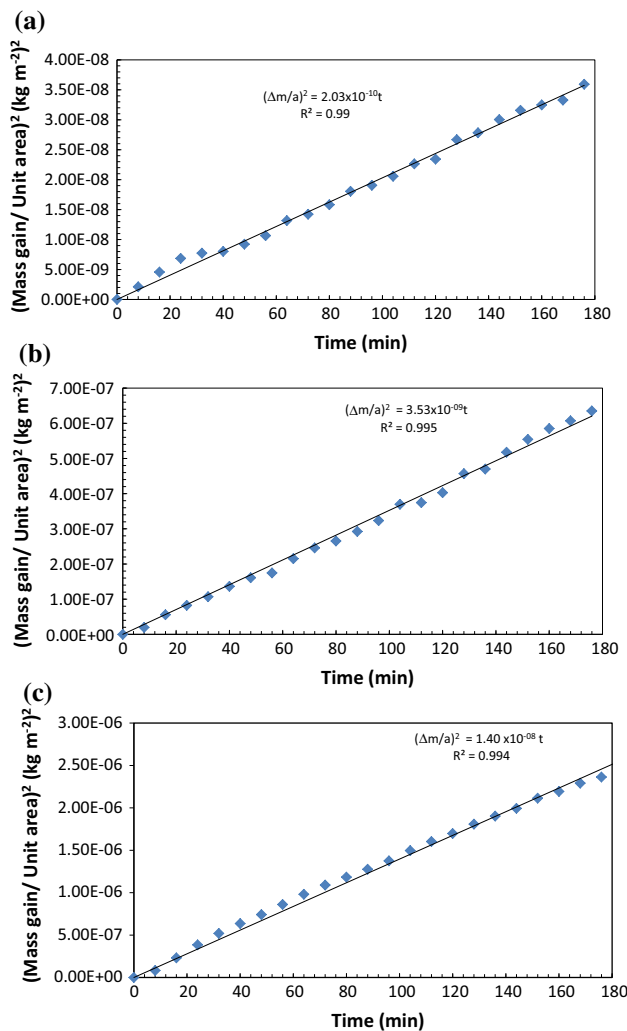
Fig. 5 Example plots of $(\Delta m/a)^2$ versus time of exposure for 25 % Ni(Cr)–75 % Cr$_3$C$_2$ coatings at **a** 650 °C **b** 700 °C and **c** 800 °C. On these plots the best-fitting straight line through the origin is given along with the coefficient of determination R^2

Cr$_2$O$_3$ peaks due to oxidation primarily on the coating surface. Looking at the ratio of the Cr$_2$O$_3$ to Ni peak heights in the XRD patterns, the coating heat treated at 800 °C had higher oxide thickness on the coating top surface compared with the coatings heat treated at 700 °C. There is no evidence in these patterns for the formation of other chromium carbide phases such as Cr$_7$C$_3$ or Cr$_{23}$C$_6$. Coating samples were also examined by XRD after the top surface oxide had been removed by grinding and these

Temperature (°C)	Parabolic rate constant, k (kg^2 m^{-4} min^{-1})			Mean value
	Experiment #1	Experiment #2	Experiment #3	
650	2.03×10^{-10}	2.41×10^{-10}	1.66×10^{-10}	2.03×10^{-10}
700	3.53×10^{-9}	4.35×10^{-9}	2.63×10^{-9}	3.50×10^{-9}
800	1.40×10^{-8}	8.98×10^{-9}	2.31×10^{-8}	1.54×10^{-8}

Table 1 Parabolic oxidation rate constants obtained from oxidising 25 %NiCr–75 %Cr$_3$C$_2$ HVOF sprayed coatings at the temperatures shown in air

Fig. 6 Arrhenius-type plot of ln k versus $10^4/RT$ for oxidation of the 25NiCr–75Cr$_3$C$_2$ coating with minimum and maximum values of k (see Table 1) as *error bars*. The slope of the best-fitting line, obtained from the linear regression equation is shown on the legend with R^2 value
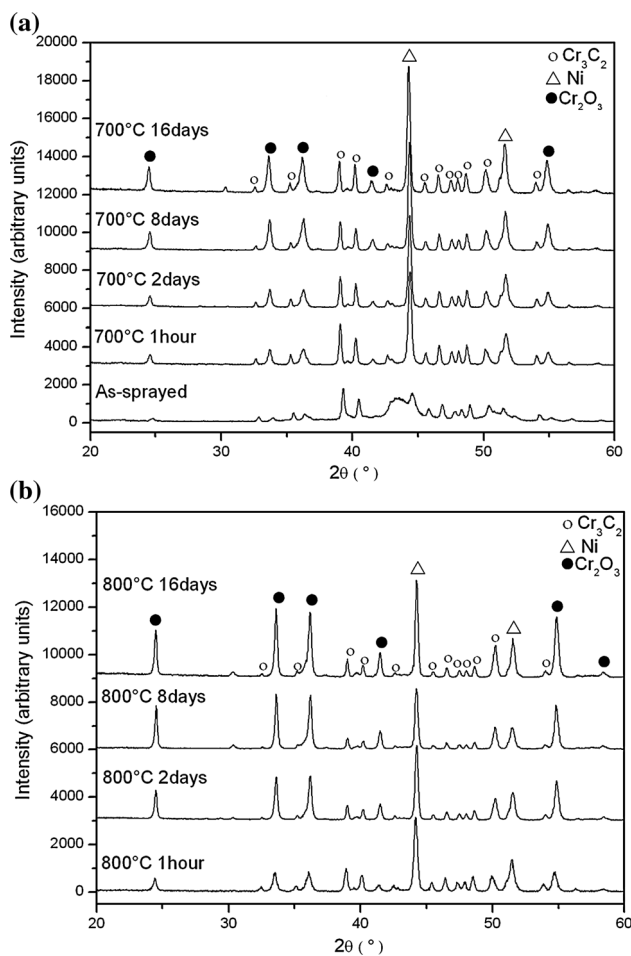
Fig. 7 XRD spectra obtained from the top surface of coatings oxidised at **a** 700 °C and **b** 800 °C with different exposure times ranging from 1 h to 16 days. The XRD spectrum of the as-sprayed coating is shown for reference on **a**

samples confirmed that carbides other than Cr$_3$C$_2$ could not be detected. These findings are in line with those reported in several other studies where Cr$_3$C$_2$ remained the dominant carbide phase [30–34].

Microstructure of the coating

Figure 8a–d shows the microstructure of polished cross-sectioned 25 %NiCr–75 %Cr$_3$C$_2$ coatings which were heat treated at 700 °C for 1 h, 2 days, 8 and 16 days, respectively. When compared with Fig. 3b it is evident the BSE images reveal that sub-micron precipitates have formed in regions that were Ni-rich matrix in the as-sprayed coating. With increasing exposure time the precipitates coarsen and form a semi-continuous network within the Ni-rich matrix which surrounds the angular carbides (labelled C); the latter are Cr$_3$C$_2$ inherited from the feedstock powder splats. Although the sub-micron carbides cannot be analysed by SEM/EDX the evidence from the XRD patterns is that these precipitates are also the Cr$_3$C$_2$ phase, which is in line with the findings of other work [30–34]. It is also apparent that in this near-surface region of the coating, localised areas of porosity developed in regions associated with the larger angular carbide particles. It would appear that, compared with the as-sprayed condition, there is more porosity found following oxidation and that the pores are larger. However, this could not be quantified. The BSE images of the polished, cross-sectioned 25 %NiCr–75 %Cr$_3$C$_2$ coating which were heat treated in air at 800 °C from 1 h up to 16 days are shown in Fig. 9 and reveal similar features to those of Fig. 8. The main difference appears to be that more porosity formed near to the surface and the precipitated carbides appear to be marginally coarser at this temperature. Also, the degree of coalescence and bridging of the blocky carbides appears greater in the BSE images of the 800 °C samples.

Oxide scale characterization: cross-sectional morphology

In Fig. 8a, a very thin and discontinuous oxide layer, which is less than ∼1 μm in thickness is seen to have formed on the top of the coating surface following 1 h exposure at 700 °C. With increasing exposure time the oxide layer increased in thickness but a continuous oxide layer did not develop until more than 8 days exposure. The sample exposed for 16 days shows an approximately 2-μm-thick oxide layer on the top of the coating (Fig. 8d). The composition of region O in Fig. 8d, as determined by EDX analysis, showed the following composition: 64 % O, 28 % Cr and 8 % Ni (at.%). It should be noted that the semi-quantitative nature of the EDX analysis cannot reliably measure the percentage of oxygen in the phase.

In Fig. 9a, oxide scale started to form with a thickness of ∼1 μm on the top of the coating following 1 h of heat
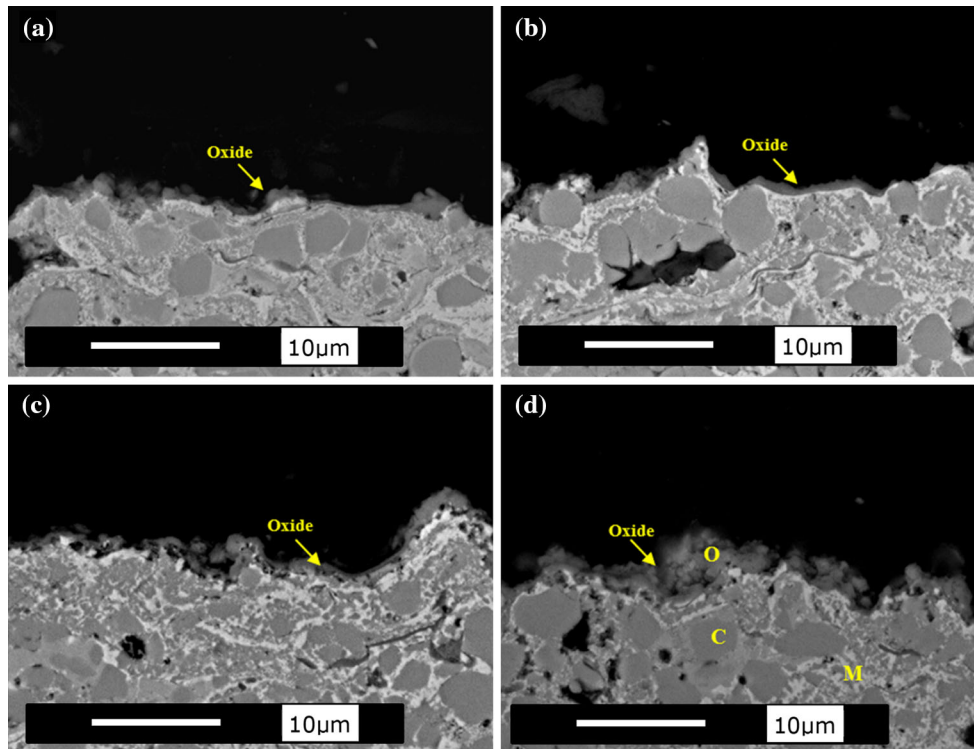
Fig. 8 BSE cross-sectional images of the NiCr–Cr$_3$C$_2$ coatings heat treated at 700 °C taken from the near surface region with different exposure times **a** 1 h, **b** 2 days, **c** 8 days and **d** 16 days with oxide labelled O, carbide region C and region M that were Ni-matrix
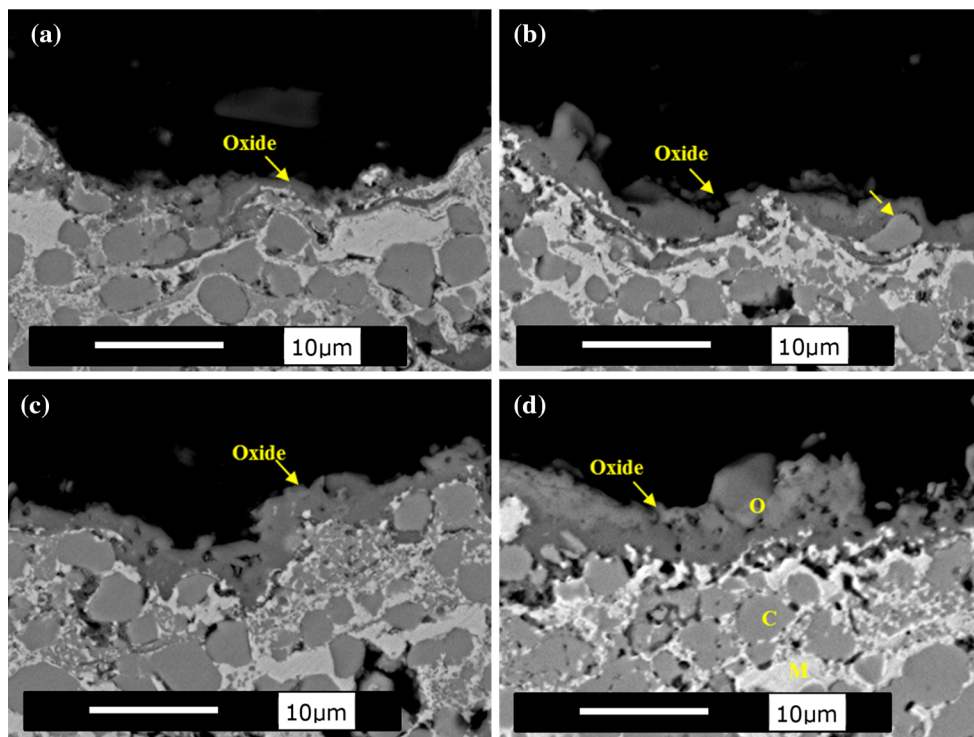
Fig. 9 BSE images showing a cross-sectional view of the NiCr–Cr$_3$C$_2$ coatings heat treated at 800 °C with different exposure times **a** 1 h, **b** 2 days, **c** 8 days and **d** 16 days

treatment. The oxide layer appears to be growing over both the Ni-rich matrix and the carbides following 2 days heat treatment (Fig. 9b). The thickness of the oxide layer increased to ∼4 μm for the coating sample after 16 days exposure as seen in Fig. 9d. The chemical composition of the oxide determined by EDX spot analysis at point O was 65 % O, 29 % Cr and 7 % Ni (at.%). The carbides on the top surface of the coating are seen to be engulfed by the oxide as noted in the area marked with the discontinuous arrow in Fig. 9b. EDX analyses of phase compositions in Fig. 9d (excluding carbon) show that region M is a Ni solid solution (18 % Cr, 82 % Ni.) whilst region C, grey blocky particles, corresponds to the carbide phase with a composition (excluding carbon) of 95 % Cr and 5 % Ni. It is also evident that considerable porosity forms underneath the oxide scales in the sample oxidised at 800 °C.

Oxide scale characterization: top surface scale morphology

The typical surface topography of the as-sprayed coating microstructure observed in the SEM using secondary electron imaging mode is shown in Fig. 10a. The coating has a rough surface and the spherical particles of the partially melted, agglomerated and sintered powder feedstock which had impacted on the surface result in an irregular distribution of a range of particle sizes. The EDX spectrum of the region on the top surface of the as-sprayed coating shows mainly Cr and Ni without any detectable oxygen. The surface topography of the coating after 1 h of oxidation in air at 700 °C shows needle-like oxide growth on the surface. A number of bulbous particles (A) which contain oxygen (as detected in the EDX spectrum) and plate-like crystals (B), which are the projections of the oxide phases in the early stage of development, are also seen. After 8 days heat treatment at 700 °C the small plate-like crystals have changed into fine cubic crystals. The EDX spectrum of these particles shows a high level of oxygen. The Ni peak in the EDX spectrum has decreased and nearly disappeared in the 8 day sample. As the chromium oxide thickened the EDX signal from the underlying nickel matrix decreased (the electron beam cannot penetrate more than about 3 μm in the material at the 20 kV operating voltage employed).

The surface of the oxidised coating after 1 h heat treatment at 800 °C in Fig. 10d shows that the surface is
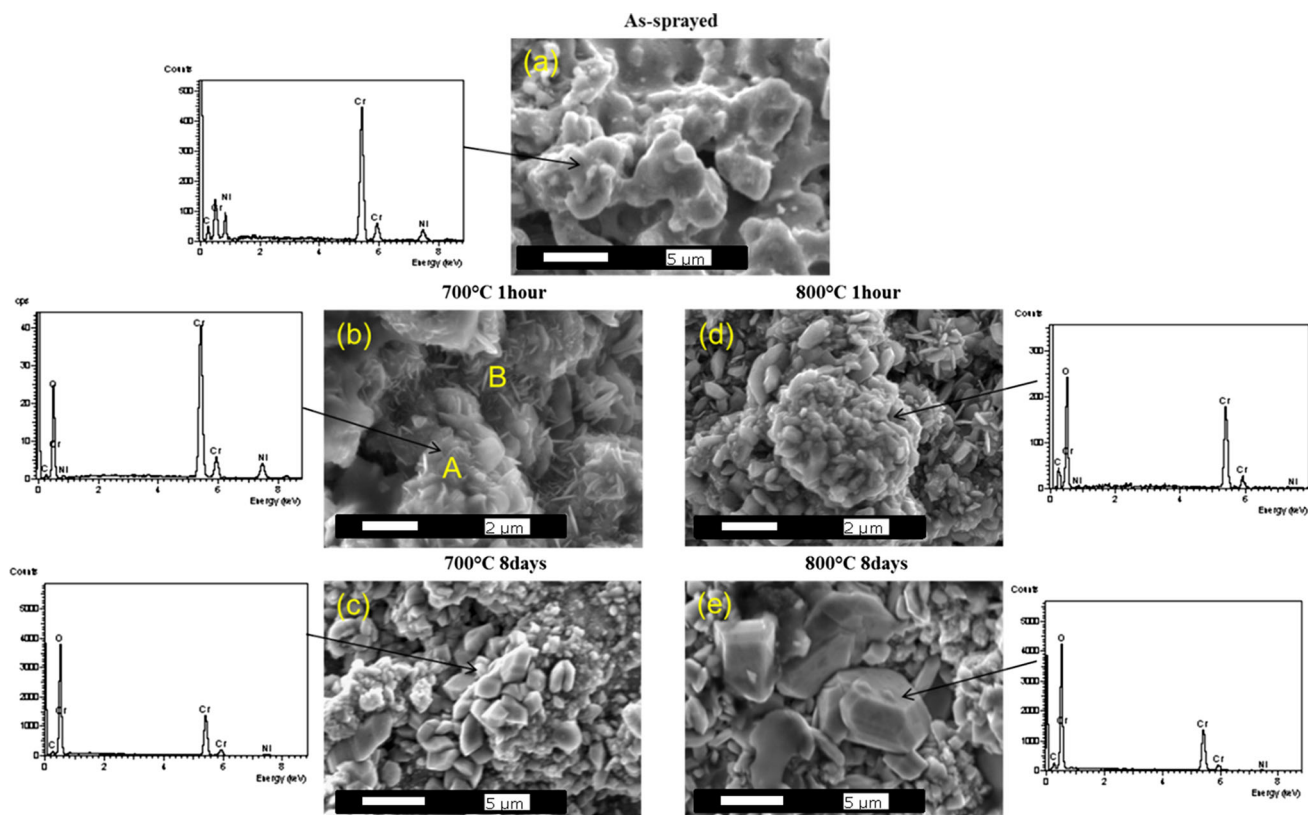
Fig. 10 SEM images of the top surface morphology of 25 %NiCr–75 %Cr$_3$C$_2$ coatings following different high-temperature exposures: **a** as-sprayed coating a; **b, c** oxidised at 700 °C for 1 h and 8 days in air respectively; **d, e** oxidised at and 800 °C for 1 h and 8 days, respectively. The EDX spectra illustrate the elements detected on top surface of each coating by point analysis

mostly covered with bulbous-shaped crystals with a small fraction of sub-micron plate-like crystals. The EDX spectrum from the bulbous-shaped crystals shows a high content of oxygen and chromium. After 8 days heat treatment at 800 °C, the size of these grains became larger developing to 10 μm in size at places. A high oxygen and chromium content are detected in the EDX spectrum. The oxide grown at 800 °C is more uniform and thicker compared to the oxide developed at 700 °C (hence no trace of Ni was detected by EDX analysis from the top surface).

Discussion

Evolution of coating microstructure

The as-sprayed microstructure consists of Ni- rich matrix containing dispersed Cr_3C_2 and the grey scale contrast of the matrix in the BSE image implies a variation in matrix composition. This suggests varying amounts of dissolved Cr and C which are dependent on the precise thermal history of individual powder particles in the high-temperature gas jet of the HVOF gun. During spraying, the Ni(Cr) matrix in the agglomerated and sintered powder, with a melting point around 1430 °C [35, 36], will partially or fully melt depending on the precise thermal history of a powder particle in the gas jet. There will then be some dissolution of the angular Cr_3C_2 into the molten Ni(Cr) creating a supersaturated Ni(Cr,C) solution and carbide particles which appear rounded and less angular. According to the phase diagram proposed by Velikanova et al. [36] there is a low-melting-point eutectic reaction between Ni(Cr,C) solid solution and Cr_3C_2 at approximately 1255 °C. If this is the case, then formation of a liquid phase could occur at the matrix-carbide interface during powder particle heating in the hot gas jet of the spray gun. This could lead to a longer time being available for carbide dissolution during spraying since the eutectic temperature is 175 K lower than the onset of melting of Ni–20 wt% Cr.

Whilst neither the coating carbon content nor the volume fraction of Cr_3C_2 in the coating were measured in this study, it is evident that the carbide volume fraction is less than the nominal value of 80 vol% which would be expected based on the nominal chemical composition of the powder which is 25 wt% Ni20Cr–75 wt% Cr_3C_2 (equivalent to 70.5 wt% Cr–20 wt% Ni–9.5 wt% C). In the previous work, chemical analysis of coatings similar to those of the present study showed that the carbon level in a coating was typically around 8 wt% C, i.e. significantly lower than in the feedstock powder [37]. Li et al. [38] also measured carbon loss in HVOF sprayed NiCr–Cr_3C_2 coatings and their experiments demonstrated that, in the main, the decrease in carbon content of the coating can be attributed to loss of carbide particles because a proportion rebound from the surface during spray deposition. Therefore, it seems likely that a similar loss of carbide particles occurred in the present study although it has not been quantified. Overall, the microstructural features observed in the coating are similar to those reported previously, e.g. references [23–27]. However, it is important to note that the coating microstructure depends critically on the type of feedstock powder employed, e.g. blended, sintered and crushed, agglomerated and sintered or plasma densified, as well as on numerous thermal spray process parameters.

During the isothermal high-temperature exposure of the samples the grey contrast regions seen in the BSE images of the as-sprayed coating have disappeared and fine scale carbides have precipitated (see Figs. 8, 9). Also the carbide peaks in the XRD spectra have sharpened with the disappearance of the halo feature between approximately $2\theta = 42.5°$ and 44.5°. The halo feature, which can be attributed to amorphous or nanocrystalline microstructural regions, is seen to disappear (Fig. 7) within the first hour of heating. Neither Cr_7C_3 nor $Cr_{23}C_6$ formed during the high-temperature exposure. The precipitation of fine scale Cr_3C_2 can be attributed to the presence of a Ni-rich matrix phase, supersaturated with Cr and C, which forms when powder particles strike the substrate and rapidly cool and solidify. On subsequent heating, the supersaturated matrix will tend to decompose to a more stable state giving rise to sub-micron Cr_3C_2 precipitates in a less supersaturated matrix. The observations on the phase evolution of the coating during high-temperature exposure are broadly in line with the results reported in several other studies [30–34]. Thus, when considering the mechanism of oxidation of these coatings, it is important to consider how matrix regions with sub-micron carbide precipitates and micron-sized angular carbide particles will both react with oxygen and how oxidation will proceed.

Kinetics of high-temperature oxidation of the coating

The oxidation kinetic behaviour of the present 25 %NiCr–75 %Cr_3C_2 coating are found to be parabolic for the temperatures between 650 and 800 °C as shown in Fig. 5. The average parabolic rate constants of the present coating at 650 °C is 2.03×10^{-10} kg^2 m^{-4} min^{-1}, at 700 °C is 3.50×10^{-9} kg^2 m^{-4} min^{-1} and at 800 °C is 1.54×10^{-8} kg^2 m^{-4} min^{-1} leading to an estimate for the activation energy of 226 kJ mol^{-1} over the rather limited range of temperatures investigated. There has been little work reported in the open literature on oxidation kinetic studies of these types of HVOF-sprayed coatings but there are a few related studies with which our data can be compared. These studies reported the parabolic rate

constants of coatings adhered to substrates. Ye et al. [18] reported the TGA results of a Cr39Ni7C (Sulzer Metco 5241 powder) coated SS400 steel at 800 °C, which also followed a parabolic rate law. XRD studies showed that the feedstock powder contained only Cr_3C_2 and Ni(Cr) phases. The parabolic rate constant for their coated samples were 1.5–2.04 $\times$ 10^{-5} kg^2 m^{-4} min^{-1}. Kamal et al. [17] studied the high-temperature oxidation of D-gun sprayed 25 Ni(Cr)–75 Cr_3C_2 coating on Fe- and Ni-based superalloys at 900 °C. The coatings with substrates during 100 cycles also followed the parabolic rate law and had a parabolic rate constant of $\sim 10^{-8}$ kg^2 m^{-4} min^{-1}.

Oxidation kinetic studies of bulk NiCr alloys have been reported in the literature which can be compared with the oxidation behaviour of the coating matrix in this study. Calvarin et al. [39] studied the oxidation behaviour of Ni–20 %Cr single-phase alloy foils in a high sensitivity TGA at 500–900 °C and they reported that the experimental weight gain of Ni–20 %Cr sample from 700 to 900 °C follows a two-stage kinetic behaviour. The first stage obeys the parabolic law and the second stage follows the complete law (a law with a linear component and a parabolic component). The parabolic rate constants for Ni–20 %Cr at 700 °C were 3.8 $\times$ 10^{-8} kg^2 m^{-4} min^{-1} for first stage (NiO layer) and 2.6 $\times$ 10^{-11} kg^2 m^{-4} min^{-1} for the second stage (Cr_2O_3 layer) and at 800 °C was 3.6 $\times$ 10^{-7} kg^2 m^{-4} min^{-1} for first stage and 2 $\times$ 10^{-10} kg^2 m^{-4} min^{-1} for the second stage. The values from this study (Table 1) are within the values reported for the stage 1 and stage 2 constants of the Ni–20 %Cr alloy. The rate constants for the freestanding coatings in both cases are smaller than the oxidation constants of the NiO layer but larger than the oxidation constants of the Cr_2O_3 layer reported in the study by Calvarin et al. [39]. The activation energy for oxidation obtained from the freestanding coatings in the present study was found to be 226 kJ mol^{-1} from the TGA experiment. In the study by Calvarin et al. [39], the activation energy for Ni–20 %Cr was 190 kJ mol^{-1} for NiO formation and between 96 and 171 kJ mol^{-1} for Cr_2O_3 scale formation. The difference in activation energy for the freestanding coating is possibly due to the presence of chromium carbide particles in the coating and also the matrix which contains a sub-micron carbide dispersion (see Figs. 8, 9).

The influence of chromium carbides on high-temperature oxidation of nickel-based alloys have been reported using cast alloys with various amounts of carbon. Berthod [40], in a study with Ni–30 wt%Cr–0.2 wt%C and Ni–30 wt%Cr–0.8 wt%C in cast alloys showed that the oxidation kinetics increased when the carbide concentration in the alloy increased. According to Berthod [40], the activation energy for oxidation of Ni–30 wt%Cr alloy was 167 kJ mol^{-1}, for the Ni–30Cr–0.2C alloy it was 201 kJ mol^{-1} and for the Ni–30Cr–0.8C alloy it was

204 kJ mol^{-1}; which were calculated from the mass-gain curves obtained by TGA on the basis of a differential equation describing the oxidation kinetics. In the present study, the activation energy of the HVOF thermal sprayed 25 wt% Ni(Cr)–75 wt% Cr_3C_2 coating at 650–800 °C is slightly higher than the values reported in the study by Berthod [40]. This higher value could be attributed to higher carbide volume fraction in this coating.

In this present study, the short term (3 h) TGA data can be extrapolated to predict the scale growth in the long-term oxidation (384 h) test results assuming no change in mechanism. In the XRD analysis only Cr_2O_3 was detected in the exposed samples. Using the density of the Cr_2O_3 as 5220 kg m^{-3} and assuming only Cr_2O_3 is grown uniformly over the surface of the coating, the scale thickness can be predicted using the short-term TGA kinetic data. Based on those assumptions, the scale thickness at 700 °C after 1 h is 0.1 μm, after 2 days 0.6 μm, after 8 days 1.2 μm and after 16 days 1.7 μm. Now, looking at the cross section of the images of the coatings following exposure at 700 °C in Fig. 8, these calculated values are well in line with the observed thicknesses (sub-micron to 2 μm). Similarly, using the same methodology, the scale thickness of the coating following exposure at 800 °C can be calculated as follows: 0.2 μm after 1 h, 1.2 μm after 2 days, 2.4 μm after 8 days and 3.4 μm after 16 days. A direct comparison can be made to the oxide scale thickness of the coatings shown in Fig. 9. The scale growth seen on the coating after 16 days is around ~ 4 μm and the scale after 8 days is 1.5–2.5-μm thick.

Mechanisms of oxidation of the NiCr–Cr_3C_2 coating: a comparison with Ni–Cr alloys

The oxidation of Ni–20 %Cr alloys has been extensively studied since the mid-70 s due to their importance relating to high-temperature applications [41]. Typically in a Ni–20 %Cr alloy NiO, $NiCr_2O_4$ and Cr_2O_3 are all formed during high-temperature exposure [41–43]. The striking difference in this study is that evidence for NiO or $NiCr_2O_4$ was not obtained in the XRD scans following exposure up to 16 days at both temperatures and only Cr_2O_3 could be detected. However, the limit of detection of the XRD method employed is typically 1–2 wt%, so very small quantities of NiO or $NiCr_2O_4$ could have formed. Therefore, further work is needed, using techniques which are more surface sensitive such as Raman spectroscopy or grazing angle X-ray diffraction, to clarify whether nickel oxide or spinel oxide are present.

In a bulk Ni–20 %Cr alloy, both NiO and Cr_2O_3 are formed and grow laterally covering the entire surface. Both oxides grow outward, and the NiO grows faster than Cr_2O_3 [43]. However, due to the greater stability of Cr_2O_3, it will

grow until the surface is covered with a continuous layer. The NiO will react with Cr_2O_3 to form the $NiCr_2O_4$ spinel.

$$NiO + Cr_2O_3 = NiCr_2O_4. \qquad (2)$$

Therefore, there is a continuous layer of Cr_2O_3 adjacent to the metal surface and an outer layer consisting essentially of spinel. Ni^{2+} ion diffusion is much slower through the $NiCr_2O_4$ spinel than it is through NiO, $NiCr_2O_4$ in the scale acts as a diffusion barrier for migrating Ni^{2+} ions [29]. However, in alloys with increasing amounts of Cr present in them only minor amounts of nickel-containing oxides are found in the scale. Selective oxidation of chromium takes place in alloys with more than 20 wt% Cr [41]. A TEM study of oxidation in model Ni-10 %Cr, Ni–20 %Cr and Ni–30 %Cr alloys by Ul-Hamid reported that Cr_2O_3 was the only oxide found in the scale when Ni–30 %Cr was oxidised at high temperatures [44]. The shift towards a single-phase Cr_2O_3 scale from multi-layered NiO, $NiCr_2O_4$ spinel and Cr_2O_3 scale occurs at chromium concentrations beyond 20 wt%.

In the present study, the two-phase coatings with large angular Cr_3C_2 particles retained from the spray powder and a matrix which is possibly saturated with Cr and C with sub-micron Cr_3C_2 precipitates formed during high-temperature exposure would appear to act more like alloys with higher Cr content than Ni–20 %Cr in that there was no evidence, from the XRD patterns, of $NiCr_2O_4$ spinel or NiO.

Mechanisms of oxidation of the NiCr–Cr_3C_2 coating: a comparison with other cermet systems

There has been relatively little work on two-phase alloys containing carbide particles although Durham et al. [45] have studied in detail the Co-Cr-C system which has some similarities with the cermet coatings of the present study. In their study, reaction rates were insensitive to carbon and when silicon was present chromium oxidised selectively leading to protective scale of Cr_2O_3. Under these circumstances chromium carbide beneath the alloy surface dissolved and chromium diffused to the surface, sustaining the growth of protective Cr_2O_3. They reported that whether the chromium carbide can supply chromium and support protective chromia growth depends on surface oxide nucleation. They suggested that the size of the carbides is important in protecting the alloy from high-temperature oxidation. In another study, Durham et al. [46] investigated fine and coarse chromium carbides and it was reported that fine carbides can dissolve fast enough to provide the chromium flux needed to form and maintain the growth of Cr_2O_3 scales. The high surface area to volume ratio of finely dispersed particles facilities the formation of protective Cr_2O_3 scales as more chromium can be released from smaller particles on a per volume basis. As the time

progresses during isothermal heat treatment the dissolution of the large carbides take place. In the present study, a bimodal distribution of chromium carbide is found which is composed of large angular chromium carbides retained from the powder and the fine carbides precipitated in the matrix. Both the fine and the coarse chromium carbides are expected to be available for dissolution to provide the chromium flux needed to form and maintain Cr_2O_3.

A further important consideration is the mechanism by which the coarse Cr_3C_2 might oxidise. Within the present coating there are coarse Cr_3C_2 particles which are inherited from the original feedstock powder i.e. were not dissolved or oxidised or rebounded from the surface during the thermal spray process. Studies on the high-temperature oxidation of chromium carbides are quite limited [19, 47]. It has been reported that oxidation of the Cr_3C_2 leads to decarburization to form stable films of Cr_2O_3 at high temperatures around the carbide particles, inhibiting further oxidation [19, 47]. From the SEM cross sections, a continuous external Cr_2O_3 layer was seen on the outside of the chromium carbide particles, within which the transport of chromium and oxygen occurs. Specifically in Fig. 9, it is noticed that the large carbides are engulfed with oxide following isothermal oxidation at 800 °C. From previous studies on oxidation of chromium, [48, 49] it was shown that the chromium diffusion is faster than oxygen diffusion in Cr_2O_3 below 1100 °C. Tsai et al. [50] calculated the oxygen and chromium bulk diffusion coefficient (DB) and grain boundary diffusion coefficient (D_{gb}) in Cr_2O_3 scales. The oxygen DB and D_{gb} at 800 °C are 2.6×10^{-22} and 5.9×10^{-17} m^2 s^{-1} and the chromium DB and D_{gb} values are 5.9×10^{-22} and 1.1×10^{-16} m^2 s^{-1}, respectively. The scale growth is dominated by counter-current diffusion of oxygen and chromium and the main phenomenon being grain boundary diffusion. Similarly in Ni–Cr matrix, growth of the Cr_2O_3 oxide occurs by the diffusion of Cr outwards to the oxide-gas interface and, as Cr migrates outwards from the matrix, pores can form just below the Cr_2O_3 oxide layer which could explain the observation of sub-scale porosity in the present samples.

One explanation for the growth of Cr_2O_3 scales on chromium carbides is that as the chromium diffuses through the initial chromia scale and forms new external chromium oxide, simultaneously, carbon from chromium carbides also diffuses through the chromia scale and released as CO [17, 47]. The chemical potential gradient of carbon decreases from the carbide–scale to scale–gas interface where the rapid consumption of carbon occurs by the combustion reaction. The equation can be written as:

$$Cr_3C_2 + 3.25O_{2(g)} = 1.5Cr_2O_3 + 2CO_{(g)}. \qquad (3)$$
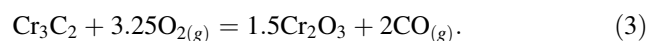
Although, it has been reported by some researchers [17] that oxidation of Cr_3C_2 leads to formation of Cr_7C_3

(orthorhombic) and $Cr_{23}C_6$ (FCC) phases at 900 °C, no such phases were detected in this study at 650–800 °C using XRD. An alternative explanation for oxidation of Cr_3C_2 has been put forward by Matthews et al. [51] as a result of their study on thermally sprayed NiCr–Cr_3C_2 coating in erosion-oxidation studies at 700–900 °C. They proposed that the oxidation of the Cr_3C_2 particles within the coating occurs by an inward growing Cr_2O_3 oxide on the carbide particles. They suggested that oxygen migrates through the oxide and oxidation occurs at the carbide oxide interface. The Cr_2O_3 formed on Cr_3C_2 is supposedly permeable to CO which escapes to the surroundings. In their oxidation study, a continuous oxide layer that was adherent to both coating phases (i.e. matrix and carbides) formed at 900 °C without any internal oxidation of each splat, which is in-line with our findings at 650–800 °C.

In summary, Cr_3C_2–NiCr apparently has good oxidation resistance due to the formation of the dense protective chromia layers. The chromia is capable of being formed on the Ni-rich matrix containing fine Cr_3C_2 and also on the undissolved coarse Cr_3C_2 particles giving a continuous layer. In high-temperature engineering applications, the coating relies on the formation of this protective oxide scale, and hence, the kinetic behaviour and mechanism of oxidation in air of the coating sre crucial in understanding the behaviour in more complex environment.

Conclusions

The high-temperature oxidation of the HVOF thermal sprayed 25 %Ni(Cr)–75 %Cr_3C_2 freestanding coatings was investigated using thermogravimetric analysis at 650, 700 and 800 °C. The coated samples were also heat treated for 16 days in laboratory air at 700 and 800 °C. Following exposure, the oxide scales were characterized using XRD and SEM/EDX on the sample cross section and the top surface. The following conclusions can be drawn from this study

1. The TGA study of the oxidation of 25 %NiCr–75 %Cr_3C_2 coating indicates that the specific weight gain curves follow a parabolic kinetic law at 650–800 °C. The parabolic rate constant (k) of the coatings were as follows: 2.03×10^{-10} kg^2 m^{-4} min^{-1} at 650 °C, 3.5×10^{-9} kg^2 m^{-4} min^{-1} at 700 °C and 1.54×10^{-8} kg^2 m^{-4} min^{-1} at 800 °C.

2. The analysis of the rate constant reveals that the activation energy (Q) for the oxidation of the HVOF sprayed 25 %NiCr–75 %Cr_3C_2 cermet coating is ~ 226 kJ mol^{-1}.

3. Following the exposure in the air at 700 and 800 °C, the samples mainly formed Cr_2O_3 on both the metal matrix and the angular chromium carbide phases. Also,

no other carbide other than Cr_3C_2 was detected in the XRD analysis after the isothermal oxidation tests. The carbides on the top surface of the coating were seen to be engulfed by the Cr_2O_3 following exposure.

4. A continuous chromia scale formed in both the samples oxidised at 700 and 800 °C after 16 days and the thickness of the oxide scale increased with increasing exposure temperature (~ 2 μm at 700 °C to ~ 4 μm at 800 °C). TGA data was extrapolated to predict the oxide scale thickness after the long-term isothermal tests and the scale thickness values are in good agreement.

References

1. Skea J, Ekins P, Winskel M (2011) Energy 2050: making the transition to a secure low carbon energy system. Earthscan, London

2. Henry J, Zhou G, Ward T (2007) Lessons from the past: materials-related issues in an ultra-supercritical boiler at Eddystone plant. Mater High Temp 24:249–258

3. Natesan K, Park JH (2007) Fireside and steamside corrosion of alloys for USC plants. Int J Hydrog Energ 32:3689–3697

4. Tillman DA (2000) Biomass cofiring: the technology, the experience, the combustion consequences. Biomass Bioenerg 19:365–384

5. Simms NJ, Sumner J, Hussain T, Oakey JE (2013) Fireside issues in advanced power generation systems. Mater Sci Tech 29:804–812

6. Sundararajan T, Kuroda S, Itagaki T, Abe F (2013) Steam oxidation resistance of NiCr thermal spray coatings on 9Cr-1Mo Steel. Part 1. ISIJ Int 43:95–103

7. Kunioshi CT, Correa OV, Ramanathan LV (2006) High temperature oxidation and erosion–oxidation behaviour of HVOF sprayed Ni–20Cr, WC–20Cr–7Ni and Cr3C2–Ni–20Cr coatings. Surf Eng 22:121–127

8. Wang B, Shui ZR (2002) The hot erosion behaviour of HVOF chromium carbide—metal cermet coatings sprayed with different powders. Wear 253:550–557

9. Wang B, Luer K (1994) The erosion oxidation behaviour or HVOF Cr3C2-NiCr cermet coating. Wear 174:177–185

10. Matthews SJ, James BJ, Hyland MM (2007) Microstructural influence on erosion behaviour of thermal spray coatings. Mater Charact 58:59–64

11. Matthews S, James B, Hyland M (2009) The role of microstructure in the mechanism of high velocity erosion of Cr3C2–NiCr thermal spray coatings: Part 2—Heat treated coatings. Surf Coat Tech 203:1094–1100

12. Matthews S, James B, Hyland M (2009) High temperature erosion of Cr3C2–NiCr thermal spray coatings—the role of phase microstructure. Surf Coat Tech 203:1144–1153

13. Quets JM, Walsh PN, Sirinwasan V, Tucker RC (1994) The high temperature characterisation of erosion resistant detonation gun chromium carbide coating. Surf Coat Tech 68(69):99–105

14. Sidhu TS, Prakash S, Agrawal RD (2006) Hot corrosion studies of HVOF sprayed Cr3C2-NiCr and Ni-20Cr coatings on nickel based superalloys at 900 °C. Surf Coat Tech 201:792–800

15. Kamal S, Jayaganthan KF, Prakash S (2009) Evaluation of cyclic hot corrosion behaviour of detonation gun sprayed Cr3C2–25% NiCr coatings on Ni- and Fe- based superalloys. Surf Coat Tech 203:1004–1013

16. Kaur M, Singh H, Prakash S (2012) High temperature behaviour of a HVOF sprayed Cr3C2-NiCr coating. Metall Mater Trans A 43A:2979–2992

17. Kamal S, Jayaganthan R, Prakash S (2009) High temperature oxidation studies of detonation-gun-sprayed Cr3C2–NiCr coating on Fe- and Ni-based superalloys in air under cyclic conditions at 900°C. J Alloy Compd 472:378–389

18. Ye FX, Wu SH, Ohmori A (2008) Microstructure and oxidation behavior of Cr39Ni7C cermet coatings deposited by diamond jet spray process. J Therm Spray Techn 17:942–947

19. Berger LM, Vuoristo P, Mantyla T, Gruner W (1998) A study of oxidation behaviour of WC-Co, Cr3C2-NiCr and TiC-Ni-based materials in thermal spray processes. In: Proceedings 15th International Thermal Spray Conference, 25–29 May 1998, Nice, pp 75–82

20. Matthews S, James B, Hyland M (2008) Erosion of oxide scales formed on Cr3C2-NiCr thermal spray coatings. Corros Sci 50:3087–3094

21. Matthews S, James B, Hyland M (2010) The effect of heat treatment on the oxidation mechanism of blended powder Cr3C2-NiCr coatings. J Therm Spray Technol 19:119–127

22. Guilemany JM, Nutting J, Llorca-Isern N (1994) Characterisation of Cr3C2-NiCr cermet powder for high velocity oxyfuel spraying. Powder Metall 37:289–292

23. Poirer D, Legoux JG, Lima RS (2013) Engineering HVOF sprayed Cr3C2-NiCr coatings: the effect of particle morphology and spraying parameters. J Therm Spray Techn 22:280–289

24. Zimmermann S, Kreye H (1996) Chromium Carbide coatings produced with various HVOF Spray Systems. In: Proceedings of the 9th National Thermal Spray Conference, ASM International, Materials Park. pp 147–152

25. Guilemany JM, Nutting J, Llorca-Isern N (1996) Microstructural examination of HVOF chromium carbide coatings for high-temperature applications. J Therm Spray Technol 5:483–489

26. Guilemany JM, Calero JA (1997) Structural characterization of chromium carbide nickel chromium coatings obtained by HVOF-spraying. In: Berndt CC (ed) Thermal spray: a united forum for scientific and technological advances. ASM International, Materials Park, pp 717–721

27. Wirojanupatump S, Shipway PH, McCartney DG (2001) The influence of HVOF powder feedstock characteristics on the abrasive wear behaviour of CrxCy–NiCr coatings. Wear 249:829–837

28. He J, Ice M, Lavernia E (2000) Synthesis of nanostructured Cr3C2-25(Ni20Cr) coatings. Metall Mater Trans A 31:555–564

29. Birks N, Meier GH, Pettit FS (2006) Introduction to the high-temperature oxidation of metals, 2nd edn. CUP, Cambridge

30. Matthews S, Hyland M, James B (2003) Microhardness variation in relation to carbide development in heat treated Cr3C2–NiCr thermal spray coatings. Acta Mater 51:4267–4277

31. Suegama PH, Espallargas N, Guilemany JM, Fernandez J, Benedetti AV (2006) Electrochemical and structural characterization of heat treated Cr3C2-NiCr coatings. J Electrochem Soc 153:B434–B445

32. Natali-Sora I, Mor F, La Vecchia GM, Zocchi M (1998) Structural Changes in high velocity oxy fuel sprayed Cr_3C_2/NiCr 75/25 coatings after annealing treatments. Mater Sci Forum 278–281:520–525

33. Guilemany JM, Miguel JM, Vizcaino S, Lorenzana C, Delgado J, Sanchez J (2002) Role of heat treatments in the improvement of the sliding wear properties of Cr_3C_2-NiCr coatings. Surf Coat Tech 157:207–213

34. He J, Lavernia E (2001) Precipitation phenomena in nanostructured Cr3C2-NiCr coatings. Mater Sci Engr A301:69–79

35. Brandes EA, Brook GB (1998) Smithells metals reference book, 7th edn. Butterworth-Heinemann, Oxford, pp 11–215

36. Velikanova TYa, Bondar AA, Grytsiv AV (1999) The chromium-nickel-carbon (Cr-Ni-C) phase diagram. J Phase Equilib 20:125–146

37. Wirojanupatump S (1999) Characterisation and wear performance of HVOF sprayed Cr_xC_y coatings, PhD thesis, University of Nottingham, Nottingham, UK

38. Li C-J, Ji G-C, Wang Y-Y, Sonoya K (2002) Dominant effect of carbide rebounding on the carbon loss during high velocity oxy-fuel spraying of Cr_3C_2-NiCr. Thin Solid Films 419:137–143

39. Calvarin G, Molins R, Huntz AM (2000) Oxidation mechanism of Ni—20Cr foils and its relation to the oxide-scale microstructure. Oxid Met 53:25–48

40. Berthod P (2007) Influence of chromium carbides on the high temperature oxidation behavior and on chromium diffusion in nickel-base alloys. Oxid Met 68:77–96

41. Kofstad P (1966) High-temperature oxidation of metals, 1st edn. Wiley, New York

42. Khanna AS (2002) Introduction to high temperature oxidation and corrosion, 1st edn. ASM International, Materials Park

43. Stringer J, Wilcox BA, Jaffee RI (1972) The high-temperature oxidation of nickel-20 wt. % chromium alloys containing dispersed oxide phases. Oxid Met 5:11–47

44. Ul-Hamid A (2004) A TEM study of the oxide scale development in Ni-Cr alloys. Anti-Corros Method M 51:216–222

45. Durham R, Gleeson B, Young DJ (1998) Silicon contamination effects in the oxidation of carbide-containing cobalt-chromium alloys. Mater Corros 49:855–863

46. Durham RN, Gleeson B, Young DJ (1998) Factors affecting chromium carbide precipitate dissolution during alloy oxidation. Oxid Met 50:139–165

47. Clark JN, Glasson DR, Jayaweera SAA (1986) Oxidation of chromium carbide. Thermochim Acta 103:193–199

48. Kofstad P, Lillerud KP (1980) On high temperature oxidation of chromium: II. Properties of and the oxidation mechanism of chromium. J Electrochem Soc 127:2410–2419

49. Lillerud KP, Kofstad P (1980) On high temperature oxidation of chromium: I. Oxidation of annealed, thermally etched chromium at 800°–1100°C. J Electrochem Soc 127:2397–2410

50. Tsai SC, Huntz AM, Dolin C (1996) Growth mechanism of Cr_2O_3 scales: oxygen and chromium diffusion, oxidation kinetics and effect of yttrium. Mater Sci Eng 212:6–13

51. Matthews S, James B, Hyland M (2013) High temperature erosion-oxidation of Cr_3C_2-NiCr thermal spray coatings under simulated turbine conditions. Corros Sci 70:203–211